Mechanics of Materials 151 (2020) 103611

Contents lists available at ScienceDirect

Mechanics of Materials

journal homepage: www.elsevier.com/locate/mecmat

Research paper

A finite deformation Cosserat continuum model for uncured carbon fibre composites

Amir Hosein Sakhaei [a,*], Samuel Erland [b], Timothy J. Dodwell [b,c]

[a] School of Engineering and Digital Arts, University of Kent, Canterbury, UK
[b] College of Engineering, Mathematics & Physical Sciences, University of Exeter, Exeter, UK
[c] The Alan Turing Institute, London, NW1 2DB, UK

ARTICLE INFO

Keywords:
Composite process modelling
Higher order mechanics
Cosserat continuum
Nonlinear finite elements

ABSTRACT

A new three-dimensional, finite deformation Cosserat continuum model for the elastic response of uncured carbon fibre composites is presented. The new composite process model captures the bending contribution of bundles of fibres at the microscale within a mesoscale continuum description of a composite ply. This is achieved by introducing higher-order, independent rotational degrees of freedom into the continuum formulation. This paper demonstrates the inclusion of such mechanics is essential to accurately model various bending responses induced during typical composite manufacturing processes. This includes large deformation forming, finite strain consolidation and wrinkling (the formation of an unwanted defect). If such mechanics are not included, the literature demonstrates the resulting finite element solutions have a pathological dependence on the mesh size. As a result, simulations require users to fit mesh-dependent material parameters, which limits confidence in their predictive capabilities. The Cosserat continuum, which can be seen as a form of the regularised continuum model, overcomes these challenges. In particular, this paper presents details of the finite element formulation of the new continuum model within a nonlinear Taylor–Hood Cosserat Element. Implementation details of embedding this new element within the commercial code Abaqus are given, alongside a series of increasingly complex validation simulations. Notably, the examples include modelling the formation of internal fibre wrinkles and large deformation forming, which involves complex ply-to-ply and tool-to-ply contact. The paper concludes by describing: (1) how the elastic Cosserat model can be integrated into existing large deformation process models in the literature. The approach set out readily allows researchers to include the important effects of resin flow, cure kinetics and temperature distribution, not considered in this contribution, and (2) how it is envisaged that the ply scale model can be naturally scaled up to large laminate scale simulation using mathematical upscaling techniques.

1. Introduction

1.1. Motivating industrial challenge in composite manufacturing and process modelling

In order to meet demands for increased production rates of composite components, manufacturers are forced towards highly automated production processes; of which the most common are Hot Drape or Double Diaphragm Forming (HDF or DDF) and Automated Fibre Placement (AFP). However, such processes come with an increase in the likelihood of severe manufacturing induced defects (e.g. wrinkles Dodwell, 2015; Sandhu et al., 2018; Belnoue et al., 2016; Varkonyi et al., 2019, folds Lightfoot et al., 2013; Hallander et al., 2016 and in-plane waviness Dodwell et al., 2019) which compromise the structural integrity of the as-manufactured component (Sutcliffe, 2013). A recent strategic government paper on Composite Strategy (Composites Leadership Forum, 2016), highlights the need for the high-value manufacturing industry to *'reduce time, cost and risk to market through the use of validated simulation tools'*. The industrial drive is to utilise simulation tools to predict and design-out defects, preventing long-development cycles, reducing time to market and increasing profitability.

Various studies in the literature investigate the effect of processing parameters such as stacking sequence, cure time, and bagging configuration on the quality of the final product of autoclave process (Wang et al., 2009; Li et al., 2009; Fernlund et al., 2002). Gutowski et al. (1987) observed from the experimental measurements of the deformation mechanism of the uncured fibre composites that the uncured fibre-network can be modelled as a nonlinear anisotropic elastic material, leading to a one-dimensional compaction model for predicting

* Corresponding author.
E-mail addresses: a.sakhaei@kent.ac.uk (A.H. Sakhaei), s.erland@exeter.ac.uk (S. Erland), t.dodwell@exeter.ac.uk (T.J. Dodwell).

https://doi.org/10.1016/j.mechmat.2020.103611
Received 10 April 2020; Received in revised form 17 August 2020; Accepted 23 September 2020
Available online 28 September 2020

the transverse stiffness of the uncured unidirectional fibre bed. Later, Hubert et al. (1999) and Li and Tucker III (2002) used Gutowski's approach and developed a finite element formulation to simulate the multiple physical phenomena of resin flow, fibre bed consolidation and cure during a consolidation/autoclave manufacturing process of composite laminates. Both papers assumed the fibre bed as a bi-phasic region and developed one model for solid stress and another for resin pressure which are coupled together. Separately, Belnoue et al. (2016) developed a hyper-viscoelastic model for consolidation of prepregs motivated from biological models of muscles (Limbert and Middleton, 2004). Rather than modelling the coupled system of the resin flow and solid state deformation, the effect of the resin is captured by including a visco-elastic response of the solid material model. This model has been extended to explore the influence of defects and differential consolidation (Belnoue et al., 2017, 2018; Varkonyi et al., 2019).

1.2. Higher order continuum models for composite manufacturing

A fundamental assumption of the above mentioned models is that the materials exhibit a characteristic length scale of the variations in the stress field much greater than the size of a representative volume of that material (Dodwell, 2015). For such cases, stresses may be considered uniform over that element, and homogenised properties can be rigorously derived as the length scale of the heterogeneity vanishes (Pavliotis and Stuart, 2008). Yet, by design, a composite material consists of stiff, finite size, elastic inclusions, within a relatively compliant resin matrix. In their uncured (pre-manufactured) state the contrast between fibre and matrix is very large. As a result, under a general deformation state the stress field varies over a length scale proportional to the fibres. In other words, the individual fibres (or a collection/bundle of them) to some degree deform and bend independently, and with this carry localised bending moments. The consequence of not including the local contributions of fibres bending is that the resulting bending mechanics become pathologically mesh dependent when discretised. In particular this is highlighted by Li and Tucker III (2002). They observed the formation of wrinkles in the corner radius of a thick composite part under consolidation. Yet, as shown in Li and Tucker III (2002, Fig. 7), they predicted wrinkle wavelengths precisely equal to the finite element mesh size.

Classically a number of approaches have been proposed which enrich the continuum description to capture the internal bending mechanics. Perhaps the most classical of which is the theory of the Cosserat brothers (Cosserat and Cosserat, 1909). In a Cosserat continua, continuum models are enriched with three additional, independent rotational degrees-of-freedom. The spatial gradients of these rotations give internal curvature measures, which form work conjugates to the resulting internal bending moments. In the mathematical formulation this requires equilibrium of not only forces, but also of bending moments within any finite size volume (Dodwell, 2015, Eq. 6). Therefore, the connection between curvatures and bending moments per unit volume introduces an internal 'bending modulus' to the material description. Since this represents a bending stiffness per unit volume, such continuum models inherit a *characteristic length* into the three dimensional constitutive formulation.

Experimental tests by the authors (Erland, 2017), characterised the elastic 'bending stiffness' of a single composite ply. Tests demonstrate the length dependency of the material parameters. Single plies of three different lengths were tested in a single cantilever (i.e. clamped–clamped) Dynamic Mechanical Analysis (DMA) setup. In each case, one end of the ply is clamped and cyclically displaced whilst the other is clamped and fixed. The load is recorded over a sweep of increasing temperatures and using standard DMA analysis a temperature dependent elastic storage modulus for the material is obtained. The output of these experiments are shown in Fig. 1. The results clearly show a length dependent material modulus which is counter intuitive. The key point is that if this characteristic length and internal bending mechanic is

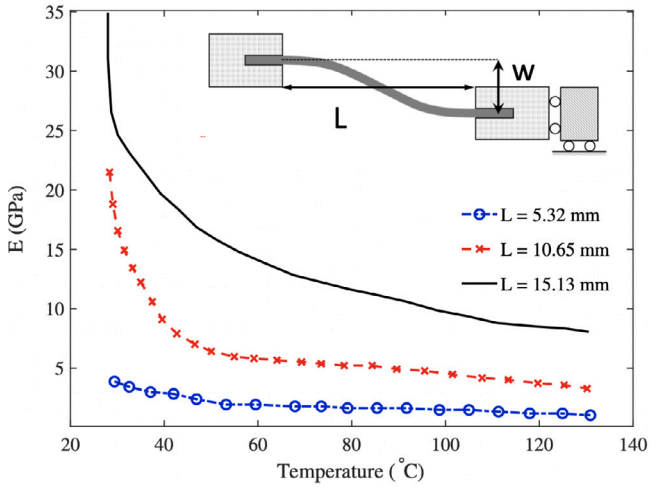

Fig. 1. Dynamic Mechanical Analysis (DMA) experiment results showing a length dependency material storage modulus, inset shows experimental setup with L representing sample length and w vertical deformation of sample.

not included, the choice of material parameters will become dependent on the mesh (or length of sample). This renders a mesh convergence study meaningless, and the parametrisation of a model is intricately coupled to the discretisation. This pathological mesh dependence for materials with internal length scales is well documented in other fields, most notability in modelling of shear bands, kink bands and folding of layered and granular media (Forest, 1998; Forest et al., 2000; Tejchman and Wu, 1993; Adhikary and Dyskin, 1997; Mühlhaus et al., 2002; Froiio et al., 2006; Hunt et al., 2013; Bigoni and Gourgiotis, 2016).

1.3. The contribution of this paper

Whilst there is an increasing realisation that higher-order mechanics should play an integral role in composite process modelling, the uptake has been relatively slow. The authors in part believe this is because existing studies in the literature are mainly mathematical (Spencer and Soldatos, 2007; Dodwell, 2015), rather than considering the practical challenges of developing and implementing models for real 3D manufacturing processes. For example, Spencer and Soldatos (2007) developed a model for fibre-composites by incorporating the fibre bending stiffness effect through a new strain–energy functional dependent on the gradient of the fibre direction. Yet, this contribution did not develop a higher order finite element discretisation to perform numerical simulations for general three-dimensional cases. Moreover, it was benchmarked for only significantly simplified analytical cases. The other researchers such as Belnoue and Hallett (2020) and Sachs and Akkerman (2017) also explained about the importance of bending behaviour of single/stack of plies during the composite forming process. They presented different methods to characterise this behaviour and implemented this effect though the constitutive model of the composite. Dodwell (2015), developed a weakly nonlinear Cosserat model at the laminate scale (multiple plies), which demonstrated its suitability for efficiently capturing the formation of wrinkling defects. However, the material formulation was simplified to a small strain, elasto-plastic behaviour, and therefore not directly applicable to the large deformations observed under forming and consolidation processes. Most recently, Madeo et al. (2015), Boisse et al. (2018b) and Boisse et al. (2018a) have proposed adding local fibre bending stiffness to the finite element model of textile composites. The approach results in a second-gradient constitutive law for forming of thin woven textile composites embedded within a shell element. Whilst there are clear connections between the approach presented in this paper and of the approaches of Madeo et al. (2015) and Boisse et al. (2018b), their shell element formulation has

reduced applications in cases which either undergo significant through-thickness compaction, or seek to model the complex poro-mechanics mechanism of flowing resin, cure and temperature redistribution.

In this contribution we addresses some of the limitations in the literature:

- The paper derives a full 3D large deformation Cosserat model for an uncured composite material. The model which builds on a constrained Cosserat theory, is designed in a way that it can be added to the strain energy functional of any composite process model within the literature, for example Belnoue et al. (2016) or, as in this paper, the model proposed by Li and Tucker III (2002) based on the seminal work by Gutowski et al. (1987).
- This paper provides details of a practical implementation within the commercial finite element software Abaqus (Abaqus, 2014). This is achieve by developing a user defined element (UEL) (Section 3). In particular we design a Taylor-Hood, hexahedral finite element with an appropriate integration scheme, to ensure interpolation of the new Cosserat degrees of freedom and the resulting finite elements are both consistent and stable.
- The resulting class of novel finite deformation Cosserat model for composite processing modelling is demonstrated, parametrised and validated with four examples of increasing complexity (Sections 4 and 5). In these studies we consider both forming and consolidation based processes. Each study aims to highlight particular aspects which the new formulation overcomes. In particular, the new formulation demonstrates no pathological mesh dependency in predicting the bending and internal wrinkling mechanics of an uncured composite layer.

2. A finite deformation Cosserat continuum model for uncured composite materials

In this section we describe the new finite deformation Cosserat continuum model for elastic response of an uncured composite material during general manufacturing processes.

2.1. Preliminaries: Finite deformation models for composite process modelling

Large deformation composite process models are primarily split between two approaches. The first proposed by Li and Tucker III (2002), models the composite as a poro-elastic medium coupled with thermo-chemical equations to describe the curing process of the resin. In this case the model accounts for the interaction between resin flow, described by Darcy's law, and the consolidation of a hyper-elastic fibrous bed. Alternatively, Belnoue et al. (2016), model the uncured composite as a large deformation visco-elastic material, which is coupled to a similar thermo-chemical equation. This visco-elastic behaviour and the bending effect in continuous fibre reinforced thermoplastic composites is comprehensively characterised and assessed by Ropers et al. through DMA and proposed rheometer-based bending experiments (Ropers et al., 2016). Independent of this choice, both approaches neglect the bending effects of fibres, and the results of both demonstrate the dependence of results to the mesh sizes. In this contribution we describe how the hyper-elastic formulation of the fibre bed of either of such models can be adapted to overcome this scientific challenge. Since this does not effect the formulation of the resin part of the models we focus solely on the elastic effects. A discussion of the extension to account for all relevant physics (flow, cure kinetics and temperature) is given in Section 6.

Consider the material coordinates in the reference configuration as $\mathbf{X} \in \Omega_0$ and the spatial coordinates in the current (deformed) configuration as $\mathbf{x} \in \Omega$ then $\mathbf{x} = \mathbf{X} + \mathbf{u}$, where $\mathbf{u}$ is the displacement vector. Furthermore, $\mathbf{F} = \partial\mathbf{x}/\partial\mathbf{X}$ describes the deformation gradient tensor and $\mathbf{C} = \mathbf{F}^{\mathrm{T}}\mathbf{F}$ the Cauchy–Green tensor. Li and Tucker III (2002) assumed that the solid stress depends on material deformation $\mathbf{C}$ and the fibre direction in the reference configuration $\mathbf{e}^0$, and propose the strain energy functional

$$W = W(\mathbf{C}, \mathbf{e}^0) = W_0(\mathcal{L}) + \frac{E_s\phi_0}{4}(L - \ln L) + \frac{G}{2}(I_1 - 3) - G(\ln J) + \frac{K}{2}(\ln J)^2. \tag{1}$$

Here, the model parameters are: E_s the axial fibre stiffness, ϕ_0 the initial fibre volume fraction, G the shear modulus and K the bulk modulus. Furthermore, the constitutive law is defined in terms of deformation measures $I_1 = \mathrm{tr}(\mathbf{C})$ and $J = \det(\mathbf{F})$, alongside L, and $\mathcal{L}$, which are additional invariants which characterise the anisotropic behaviour in the fibre direction and through-thickness directions. These final two invariants are described as

$$L = \left(\mathbf{e}^0 \otimes \mathbf{e}^0\right) \cdot \mathbf{C} \qquad \text{and} \qquad \mathcal{L} = \left(\mathbf{n}^0 \otimes \mathbf{n}^0\right) \cdot \mathbf{C}^{-1}. \tag{2}$$

where, $\mathbf{n}^0$ is a unit vector normal to the plane of the undeformed sheet. Finally, the term $W_0(\mathcal{L})$ is a separate energy functional that captures the nonlinear response transverse to the fibres. This term is explained comprehensively in Li and Tucker III (2002), is derived from Gutowski et al. (1987), and is defined by the functional

$$\frac{\partial W_0}{\partial \mathcal{L}} = \frac{A_s}{2}\frac{\mathcal{L} - \sqrt{\mathcal{L}}}{\left(\frac{1}{\phi_0} - \frac{\sqrt{\mathcal{L}}}{\phi_a}\right)^4} + \frac{G - G_0}{2}\left(\frac{1}{\mathcal{L}^2} - \frac{1}{\mathcal{L}}\right). \tag{3}$$

This energy functional comes with additional model parameters: A_s a spring constant, ϕ_a is the maximum possible fibre volume fraction and G_0 is parameter which according to Li and Tucker III (2002) is a small portion of G introduced for numerical stability.

As for any hyper-elastic material model, the solid Cauchy stress and fourth-order Lagrangian elastic tensors can be computed from the strain energy functional, where

$$\boldsymbol{\sigma}_s = \frac{2}{J}\mathbf{F}\frac{\partial W}{\partial \mathbf{C}}\mathbf{F}^{\mathrm{T}} \quad \text{and} \quad \mathbb{C} = \frac{4\partial^2 W}{\partial \mathbf{C}^2}. \tag{4}$$

The derivation of these terms is included within Appendix.

2.2. The inclusion of higher-order bending effects within a composite process model

To present a model that incorporates the local bending effect of fibres, it is necessary to include the gradient of fibre direction in the model and hence the coupled stress at each material point (Maugin, 2017; Lakes, 1995; Askes and Aifantis, 2011). To do this we introduce a vector of Cosserat rotations $\boldsymbol{\theta}(\mathbf{X})$ at each material point. This internal rotation describes the re-orientation of the fibre direction $\mathbf{e}^0$ under deformation, allowing the introduction of the fibre curvature measure

$$\boldsymbol{\Lambda} = \frac{\partial \boldsymbol{\theta}}{\partial \mathbf{X}}. \tag{5}$$

To capture the internal, independent bending of the fibres the strain energy functional can be supplemented with an additional term, so that

$$W = W_0(\mathcal{L}) + \frac{E_s\phi_0}{4}(L - \ln L) + \frac{G}{2}(I_1 - 3) - G(\ln J) + \frac{K}{2}(\ln J)^2 + \beta\left(\underbrace{\mathbf{e}^0 \cdot \boldsymbol{\Lambda}^{\mathrm{T}}\boldsymbol{\Lambda} \cdot \mathbf{e}^0}_{:=I_6}\right) \tag{6}$$

Where in addition to the parameters already defined in (1), β is a material parameter which captures the internal bending stiffness. The adjacent term, I_6, is an invariant in terms of the fibre curvature with respect to the original fibre direction $\mathbf{e}^0$.

Remark. The equation for W (6) defines an energy density. W therefore has units of Nm per volume, i.e. N/m^2. Since Λ is a curvature, with units of $1/m$, this implies that the Cosserat bending stiffness β, has the units N. Like any bending stiffness (e.g. that of a beam) the parameter has encoded in it some intrinsic internal length scale.

Alongside this additional term to the energy functional, in our model the simplifying kinematic constraint connecting shear strains and Cosserat rotations is imposed

$$\boldsymbol{\omega} = \frac{1}{2}\boldsymbol{\epsilon}\nabla\mathbf{v}. \tag{7}$$

This is according to *constrained Cosserat theory* (Fedorova et al., 2016) which states that the spin vector (rotation rate) $\boldsymbol{\omega}$ is related to the displacement rate vector $\mathbf{v}$. Here, for a shorthand notation, $\boldsymbol{\epsilon}$ defines the perturbation tensor. This is a third order tensor ϵ_{ijk}, which takes the values either $\epsilon_{123} = \epsilon_{312} = \epsilon_{231} = 1$ or $\epsilon_{213} = \epsilon_{132} = \epsilon_{321} = -1$ otherwise the tensor returns the value 0. This modelling assumption has be shown to be valid in the cases where the shear stiffnesses parallel and orthogonal to the fibres are in high contrast, and the length scale of the thickness of individual fibres is relatively small compared to the material definition at the individual layers scale (Dodwell, 2015). For the case of uncured carbon composite plies, the fibres are extremely stiff compare with the resin, and the fibres or bundles of them are thin, so this assumption seems reasonable and is supported by the numerical results in this contribution.

By introducing the fibre curvature measure $\boldsymbol{\Lambda}$ the work conjugate, the couple stress tensor $\mathbf{m}$ can also be introduced. Therefore, the constitutive equations which define the symmetric part of Cauchy stress and the deviatoric part of couple stress are given by

$$\boldsymbol{\sigma}_{sym} = \frac{2}{J}\mathbf{F}\frac{\partial W}{\partial \mathbf{C}}\mathbf{F}^{\mathrm{T}} \quad \text{and} \quad \overline{\mathbf{m}} = \frac{1}{J}\mathbf{F}\frac{\partial W}{\partial \boldsymbol{\Lambda}}\mathbf{F}^{\mathrm{T}}. \tag{8}$$

By finding the first and second derivatives of the strain energy functional (6) (given in Appendix), the stress is given by

$$\boldsymbol{\sigma}_{(ij)} = \frac{2}{J}\mathrm{F}_{im}\left\{ -\left[\frac{A_s}{2}\frac{\mathcal{L}-\sqrt{\mathcal{L}}}{(\frac{1}{\phi_0}-\frac{\sqrt{\mathcal{L}}}{\phi_a})^4} + \frac{G-G_0}{2}\left(\frac{1}{\mathcal{L}^2}-\frac{1}{\mathcal{L}}\right)\right]\mathbf{n}^0_p\mathbf{n}^0_q\mathrm{C}^{-1}_{pm}\mathrm{C}^{-1}_{nq} + \frac{E_s\phi_0}{4}\left(1-\frac{1}{L}\right)\mathbf{e}^0_m\mathbf{e}^0_n + \frac{1}{2}G\left(\delta_{mn}-\mathrm{C}^{-1}_{mn}\right) + \frac{K}{2}\ln(J)\mathrm{C}^{-1}_{mn}\right\}\mathrm{F}_{jn}, \tag{9}$$

whilst the couple stress is defined as

$$\overline{\mathrm{m}}_{ij} = \frac{2\beta}{J}\mathrm{F}_{im}(\Lambda_{mk}\mathrm{e}^0_k\mathrm{e}^0_n)\mathrm{F}_{jn}. \tag{10}$$

By imposing equilibrium of moments the anti-symmetric part of the Cauchy stress can be calculated as

$$\sigma_{[ij]} = \frac{1}{2}\epsilon_{kji}\frac{\partial m_{lk}}{\partial x_l}. \tag{11}$$

Therefore, following calculations provided in the Appendix, the fourth-order Lagrangian elastic tensor $\mathbb{C}_\sigma$, which connects σ and $\mathbf{C}$ is computed using (4), so that

$$\begin{aligned}\mathbb{C}_\sigma = 4\Bigg(&\frac{\partial^2 W_0}{\partial\mathcal{L}^2}\left(\frac{\partial\mathcal{L}}{\partial\mathbf{C}}\otimes\frac{\partial\mathcal{L}}{\partial\mathbf{C}}\right) + \frac{\partial W_0}{\partial\mathcal{L}}\frac{\partial}{\partial\mathbf{C}}\left(\frac{\partial\mathcal{L}}{\partial\mathbf{C}}\right)\\ &+ \frac{E_s\phi_0}{4}\left(\frac{\partial^2 L}{\partial\mathbf{C}^2} - \frac{1}{L}\frac{\partial^2 L}{\partial\mathbf{C}^2} + \frac{1}{L^2}\left(\frac{\partial L}{\partial\mathbf{C}}\otimes\frac{\partial L}{\partial\mathbf{C}}\right)\right)\\ &+ \frac{G}{2}\frac{\partial^2 I_1}{\partial\mathbf{C}^2} - G\left(\frac{1}{J}\frac{\partial^2 J}{\partial\mathbf{C}^2} - \frac{1}{J^2}\left(\frac{\partial J}{\partial\mathbf{C}}\otimes\frac{\partial J}{\partial\mathbf{C}}\right)\right)\\ &+ K\left(\frac{1-\ln J}{J^2}\left(\frac{\partial J}{\partial\mathbf{C}}\otimes\frac{\partial J}{\partial\mathbf{C}}\right) + \frac{1}{J}\frac{\partial^2 J}{\partial\mathbf{C}^2}\right)\Bigg),\end{aligned}$$

likewise the fourth-order Lagrangian elastic tensor $\mathbb{C}_\mathbf{m}$, which connects coupled stress $\mathbf{m}$ to our curvatures measure Λ is given by

$$\mathbb{C}_\mathbf{m} = \frac{\partial^2 W}{\partial\boldsymbol{\Lambda}^2} = 2\beta\left(\mathbf{e}^0\otimes\mathbf{e}^0\right)\otimes\mathbf{I}. \tag{12}$$

3. Large deformation, finite strain finite element implementation in Abaqus

In this section we provide details of the finite element procedure we have implemented and used in the numerical test cases presented in Sections 4 and 5. The starting point is the derivation of the weak formulation of the Cosserat model, followed by the finite dimensional discretisation using the finite element method and finally the practical implementation details within the commercial package Abaqus (Abaqus, 2014).

3.1. Weak formulation

The starting point is to apply the principle of virtual work to derive the weak formulation of the Cosserat Continuum model by finding stationary states of the total potential energy of the system in the current (or deformed) configuration, $\mathcal{V} = \mathcal{W} - \mathcal{P}$ (strain energy minus work done by loads/moments). In order to obtain the week statement of the static equilibrium of the body, we use the virtual work equation according to Fedorova et al. (2016) and Bonet and Wood (1997) by assuming $\delta\mathbf{v}$ as an arbitrary virtual velocity and $\delta\boldsymbol{\omega}$ as an arbitrary virtual spin vector:

$$\delta\mathcal{V} = \delta\mathcal{W} - \delta\mathcal{P} = \int_\Omega\left(\sigma_{(ij)}\frac{\partial\delta v_i}{\partial x_j} + \overline{m}_{ij}\frac{\partial\delta\omega_i}{\partial x_j}\right)\mathrm{d}\mathbf{x} - \int_{\partial\Omega}\left(t_i\delta v_i + l_i\delta\omega_i\right)\mathrm{d}\mathbf{s} = 0. \tag{13}$$

Here t_i and l_i are tractions and couples (moment per unit area), respectively, acting on a surface $\mathbf{s}$ of the deformed configuration Ω.

We take a total Lagrangian formulation, in which we consider the undeformed state as a reference for computations. Therefore, to take the volume integral over the initial configuration Ω_0, we rewrite (13) by defining the symmetric Kirchhoff stress tensor $\tau_{(ij)}$ and deviatoric couple stress $\overline{\mu}_{ij}$ as $\overline{\mu}_{ij} = j\overline{\mathbf{m}}$ and $\tau_{(ij)} = j\sigma_{(ij)}$, and therefore it follows that

$$\begin{aligned}\delta\mathcal{V} = &\int_{\Omega_0}\left(\tau_{(ij)}\frac{\partial\delta v_i}{\partial X_m}\mathrm{F}^{-1}_{mj}\right)\mathrm{d}\mathbf{X} + \int_{\Omega_0}\left(\overline{\mu}_{ij}\frac{\partial\delta\omega_i}{\partial X_n}\mathrm{F}^{-1}_{nj}\right)\mathrm{d}\mathbf{X}\\ &- \int_{\partial\Omega_0}\left(t_i\delta v_i + l_i\delta\omega_i\right)\mathrm{d}\mathbf{S},\end{aligned} \tag{14}$$

and for simplicity we call the first and second terms in the right hand side of Eq. (14) as $\delta\mathcal{W}_1$ and $\delta\mathcal{W}_1$ and we have $\delta\mathcal{V} = \delta\mathcal{W}_1 + \delta\mathcal{W}_2 - \delta\mathcal{P}$. This is a system of nonlinear equations with respect to both the material and the geometry, therefore the linearisation of these equations is found in order to exploit Newton based methods. To do this we handle each of the strain energy terms $\delta\mathcal{W}_1$ and $\delta\mathcal{W}_2$ independently.

For $\delta\mathcal{W}_1$, we utilise the symmetric properties of $\tau_{(ij)}$ so that we can rewrite the first component of (14) as

$$\begin{aligned}\delta\mathcal{W}_1 &= \frac{1}{2}\int_{\Omega_0}\left(\tau : \left(\nabla_0\delta v\mathbf{F}^{-1} + \mathbf{F}^{-T}(\nabla_0\delta v)^T\right)\right)\mathrm{d}\mathbf{X}\\ &= \frac{1}{2}\int_{\Omega_0}\left(\mathbf{F}^{-1}\tau\mathbf{F}^{-T} : \left(\mathbf{F}^T\nabla_0\delta v + (\nabla_0\delta v)^T\mathbf{F}\right)\right)\mathrm{d}\mathbf{X} = \int_{\Omega_0}\left(\mathbf{S} : \delta\dot{\mathbf{E}}\right)\mathrm{d}\mathbf{X}.\end{aligned} \tag{15}$$

Here $\mathbf{S}$ is the second Piola–Kirchoff stress and $\mathbf{E}$ the Lagrangian strain. The Frèchet derivative in the direction of the displacement degrees of freedom $\mathbf{u}$ gives the first stationary condition of equilibrium states, given by

$$\begin{aligned}D\left(\delta\mathcal{W}_1\right)[\mathbf{u}] = &\int_{\Omega_0}\frac{1}{2}\left(\mathbf{F}^T\nabla_0\delta v + (\nabla_0\delta v)^T\mathbf{F}\right) : \mathbb{C}_\sigma :\\ &\left(\frac{1}{2}\mathbf{F}^T\left(\nabla_0\mathbf{u} + (\nabla_0\mathbf{u})^T\right)\mathbf{F}\right)\mathrm{d}\mathbf{X}\\ &+ \int_{\Omega_0}\mathbf{S} : \left[(\nabla_0\mathbf{u})^T\nabla_0\delta v\right]\mathrm{d}\mathbf{X}\end{aligned} \tag{16}$$

Bonet and Wood (1997, Ch. 6) provide all the intermediate steps of this calculation, and therefore it is not repeated here. Similarly, we should linearise the second term on the right hand side of Eq. (14), $\delta\mathcal{W}_2$, by taking the Fréchet derivative in the direction of the rotation degree of freedom, θ, therefore

$$D\left(\delta\mathcal{W}_2\right)[\theta] = D\left(\int_{\Omega_0}\left(\overline{\mu} : \nabla_0\delta\omega\mathbf{F}^{-1}\right)\mathrm{d}\mathbf{X}\right)[\theta]$$

$$= \int_{\Omega_0} D\overline{\mu}[\theta] : \nabla_0 \delta\omega \mathbf{F}^{-1} + \overline{\mu} : D\left(\nabla_0 \delta\omega \mathbf{F}^{-1}\right)[\theta]\, \mathrm{d}\mathbf{X}. \quad (17)$$

This can expands further to

$$D\left(\delta\mathcal{W}_2\right)[\theta] = \int_{\Omega_0} \nabla_0\theta : \mathbb{C}_{\mathbf{m}} : \nabla_0\delta\omega\mathbf{F}^{-1} + \overline{\mu} : \Big[D\left(\nabla_0\delta\omega\right)[\theta]\mathbf{F}^{-1} + \nabla_0\delta\omega D\left(\mathbf{F}^{-1}\right)[\theta] \Big]\, \mathrm{d}\mathbf{X}, \quad (18)$$

where $D\left(\mathbf{F}^{-1}\right)[\theta] = 0$ and as the virtual spin is not a function of the configuration the term $\nabla_0\delta\omega$ remains constant and $D\left(\nabla_0\delta\omega\right)[\theta] = 0$. Therefore, the second stationary condition for equilibrium states is found by

$$D\left(\partial\mathcal{W}_2\right)[\boldsymbol{\theta}] = \int_{\Omega_0} \nabla_0\theta : \mathbb{C}_{\mathbf{m}} : \nabla_0\delta\omega\mathbf{F}^{-1}\mathrm{d}\mathbf{X}. \quad (19)$$

The derivation of the weak form for the Neumann boundary conditions ($\delta\mathcal{P}$), and the resulting finite element discretisation, is given explicitly by Bonet and Wood (1997, Eq. 6.23). We avoid repeating that formulation here since within our implementation in Abaqus (Abaqus, 2014) these terms are not required, and boundary conditions are implemented in an alternative way. Further details are provided in Section 3.2.

Finally, it remains to formulate the Cosserat constraint (7) in a large deformation Lagrangian framework

$$\boldsymbol{\omega} - \frac{1}{2}\boldsymbol{\epsilon}\nabla\mathbf{v} = 0. \quad (20)$$

This Cosserat constraint could be imposed in a number of ways, the classical way using Lagrange multipliers resulting in a classical saddle point problem. In this contribution, due to implementation constraints in the commercial package Abaqus (Abaqus, 2014) a simpler penalty method is used. To implement this penalty approach, we add an additional term to the strain energy function which penalises differences in the constraint over the domain in the L_2 norm. Therefore, the augmented energy is defined $\hat{\mathcal{W}} = \mathcal{W} + \mathcal{W}_c$, where the virtual constraint energy $\delta\mathcal{W}_c$ in the initial configuration is

$$\delta\mathcal{W}_c = K_c \int_V \left(\boldsymbol{\theta} - \frac{1}{2}\boldsymbol{\epsilon}\nabla_0\mathbf{u}\mathbf{F}^{-1}\right) \cdot \left(\delta\boldsymbol{\omega} - \frac{1}{2}\boldsymbol{\epsilon}\nabla_0(\delta\boldsymbol{v})\mathbf{F}^{-1}\right) \mathrm{d}\mathbf{X} = 0 \quad (21)$$

the above form then is extended, and since $\partial\delta v$ and $\partial\delta\omega$ are independent and arbitrary, we obtain two conditions

$$K_c \int_V \left(\boldsymbol{\theta}\cdot\delta\boldsymbol{\omega} - \frac{1}{2}\boldsymbol{\epsilon}\nabla_0\mathbf{u}\mathbf{F}^{-1}\cdot\delta\boldsymbol{\omega}\right) \mathrm{d}\mathbf{X} = 0 \quad (22)$$

and

$$K_c \int_V \left(-\frac{1}{2}\boldsymbol{\theta}\cdot\boldsymbol{\epsilon}\nabla_0(\delta\boldsymbol{v})\mathbf{F}^{-1} + \frac{1}{4}(\boldsymbol{\epsilon}\nabla_0\mathbf{u}\mathbf{F}^{-1})\cdot(\boldsymbol{\epsilon}\nabla_0(\delta\boldsymbol{v})\mathbf{F}^{-1})\right) \mathrm{d}\mathbf{X} = 0. \quad (23)$$

3.2. Finite element formulation and implementation in Abaqus

In this section, we describe the implementation of the constrained Cosserat continuum model using the finite element method in Abaqus. The undeformed domain Ω_0 is discretised into a conforming finite element grid $\mathcal{T}_h$. To implement within Abaqus, a User Defined Element (UEL) is written. Internally, Abaqus assembles the global matrices and residuals, and the system of nonlinear equations are solved using a Newton scheme. To implement the UEL, the user requires to assemble the element stiffness matrices and residuals on each element $\tau \in \mathcal{T}_h$. The full implementation of the finite element code will be made available on request.

In summary of the approach taken, a finite element space is introduced on each element $\tau \in \mathcal{T}_h$, so that

$$\mathbf{u}(\mathbf{x}) = \sum_{i=1}^{20} \mathbf{u}_\tau^{(i)} \mathbf{N}_u^{(i)}(\mathbf{x}) \quad \text{and} \quad \boldsymbol{\theta}(\mathbf{x}) = \sum_{i=1}^{8} \boldsymbol{\theta}_\tau^{(i)} \mathbf{N}_\theta^{(i)}(\mathbf{x}). \quad (24)$$

Here $\mathbf{u}_\tau^{(i)}$ and $\boldsymbol{\theta}_\tau^{(i)}$ give the nodal displacements and rotations (in local numbering) on a given element $\tau \in \mathcal{T}_h$. In this contribution the displacement degrees of freedom are interpolated across each element with 20-node serendipity (quadratic) shape functions $\mathbf{N}_u^{(i)}(\mathbf{x})$, whilst rotational degrees of freedom are interpolated by 8-node linear shape functions, $\mathbf{N}_\theta^{(i)}(\mathbf{x})$. The definition of these shape functions are defined in many classical text books, for example Zienkiewicz and Taylor (1994) and a graphical representation of the Cosserat element is shown in Fig. 2. The choice of different finite element spaces for displacements and rotations is important. This is because it guarantees that within an element, rotations due to the displacements (derivatives of the displacements itself) and the Cosserat rotations are approximated with the same order of polynomial, which avoids numerical instabilities and classical issues with shear locking. This is discussed in more detail in the context for 2D Cosserat models by Dodwell (2015).

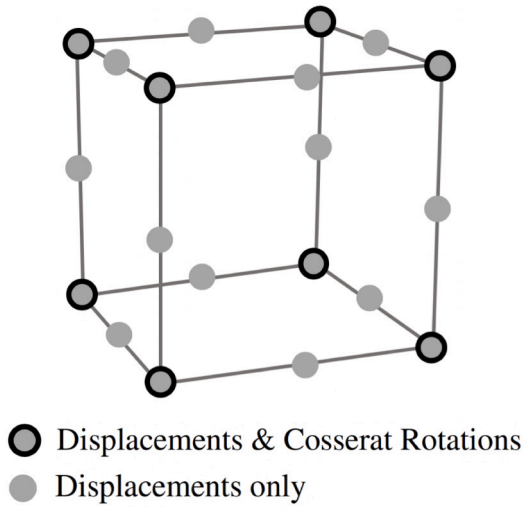

Fig. 2. 3D Cosserat finite element in their reference frame. All Cosserat rotations are interpolated with linear shape functions, whilst displacements with quadratic functions. This ensures consistency when imposing Cosserat constraint conditions (20).

The complete weak formulation of the Cosserat model is defined by the collection of Eqs. (16),(19), (22) and (23). To formulate as a system of nonlinear finite element equations, the lengthy algebraic calculations involve substituting the finite dimensional representation (24) into each of these equations. If required, the specific terms can be identified in the code which can be provided at on request. The resulting element stiffness matrix $\mathbf{K}_\tau \in \mathbb{R}^{84\times84}$ therefore has the form

$$\mathbf{K}_\tau = \begin{bmatrix} \mathbf{K}_{uu} & 0 \\ 0 & \mathbf{K}_{\theta\theta} \end{bmatrix} + \mathbf{K}_c \quad (25)$$

Where $\mathbf{K}_{uu}$ is the stiffness contribution from the classical Li & Tucker model (Li and Tucker III, 2002) as given by (16), $\mathbf{K}_{\theta\theta}$ is the submatrix arising from additional Cosserat bending terms defined by (19) and finally $\mathbf{K}_c$ are the finite element representation of the constraint Eqs. (22) and (23). The element residual of internal forces and moments is therefore the action of $\mathbf{K}_\tau$ on the solution vector for that element. It should be noted that boundary conditions are not implemented with the residual defined within the UEL. In a general finite element implementation they would be, yet in Abaqus, the simplest way to implement boundary conditions is to introduce 'ghost elements' which overlay the Cosserat elements. The 'ghost elements' are assigned near zero stiffness properties, and the nodes are constrained/tied to the nodes of the Cosserat elements. This way boundary conditions are implemented, as in any other Abaqus simulation. Furthermore, it becomes simple to implement standard contact algorithms available in Abaqus (important for forming simulations as shown in results) by using this approach. This simple work around also provides a means to visualise the solution afterwards, where visualising UEL's is not directly possible.

Table 1
Material parameters used in the simulations.

E_s	G	K	ϕ_0	ϕ_a	A_s	G_0	β	K_c
200 GPa	1 MPa	1 MPa	0.5	0.75	0.8 MPa	0.3 MPa	1	2e12

4. Benchmark examples for Cosserat formulation

This section demonstrates the new finite deformation Cosserat model for a series of increasingly complex examples. This proposed user-defined element is only used in complex three-dimensional analysis after performing careful tests for simple deformation scenarios including pure compression, tension and shear as well as observing the performance of this element under rigid body motion and rotation. This states that the balance laws are invariant under superposed rigid-body rotations. The results in this section, demonstrate the ability to capture the length dependency in the mechanics of uncured composites under bending and internal buckling deformations.

4.1. Bending mechanics of a single composite ply

The first example revisits the experimental tests which motivated this study, as presented in Fig. 1. To re-cap, the output shows the storage modulus (an elastic material constant) derived from a Dynamical Mechanical Analysis tested on a single ply. In this test, a rectangular sample is held as a cantilever, clamped at both ends with fibres running along the sample. A cyclic vertical deflection is imposed on the sample, whilst the vertical force required is recorded. The setup is shown in the inset of Fig. 1. Samples are mounted with quick curing polyurethane tabs to ensure the boundary conditions are maintained during a test. The polyurethane is demoldable within 30 minutes and mixed with milled carbon fibre to ensure it is sufficiently stiff and thermally stable. The sample length ℓ is measured between the points at which the carbon fibre sample enters the resin tab. The free-end is vertically displaced by $w = w_{\max}\sin(\omega t)$ and the required cyclic force $P = P_{\max}\sin(\omega t + \delta)$ where the force lags a time δ behind the displacement due to the viscous effects. Therefore, the rate-independent or elastic part of the force is the in-phase contribution given by $P_e = P_{\max}\cos\delta\sin(\omega t)$.

A three-dimensional model of the DMA setup is constructed in Abaqus. The ply is modelled using the new Cosserat finite element as the user-defined elements (UEL) on the ply geometry before applying the same displacement and rotational boundary conditions as the experimental test (clamped–clamped and vertical displacement at one end). To investigate the effect of length on the bending mechanics of uncured ply samples, experimental tests (using AS4-8552 composite material) and numerical simulations with three samples of different lengths ($\ell_1 = 15.13$ mm, $\ell_2 = 10.65$ mm, and $\ell_3 = 5.32$ mm) are performed. For the numerical simulations, the single-ply is discretised by approximately square elements in the plane, 13 across the width, whilst 4 through-thickness. This gives 1976, 1404, and 676 user-defined Cosserat elements for samples of lengths 15.13 mm, 10.65 mm, and 5.32 mm respectively. Material parameters for AS4-8852 are taken from other studies as provided in Erland et al. (2015) and Erland (2017), and are summarised in Table 1. This study seeks to find a suitable value of β, the Cosserat bending stiffness, which shows the new model formulation captures the experimental results accurately.

To make a comparison, the DMA output for the storage modulus, which assumes simple bending theory, is considered. Here the storage modulus is $E = P_{\max}\cos\delta\ell^3/3Iw_{\max}$ where ℓ is the length, I the second moment of area and $\tan\delta$ the dissipation factor describing how viscous the material response is. The value $P_{\max}\cos\delta$, as given by the experiment, is the elastic component of the force required to produce a deformation $w_{\max}$ at one end. Since the computational model accounts for the purely elastic response of a composite ply, this term is equivalent to the vertical reactive load R which can be calculated from the numerical simulations. From the numerical simulations, for comparison, an approximation of storage modulus $\hat{E}(\ell_i) = R\ell_i^3/3Iw_{\max}$ can be calculated. Whilst it is clear that the assumption of simple bending theory is wrong, since if valid the storage modulus of the material would be independent of sample length, the quantity $\hat{E}$ provides a simple metric by which the outputs from simulations and experiments can be compared.

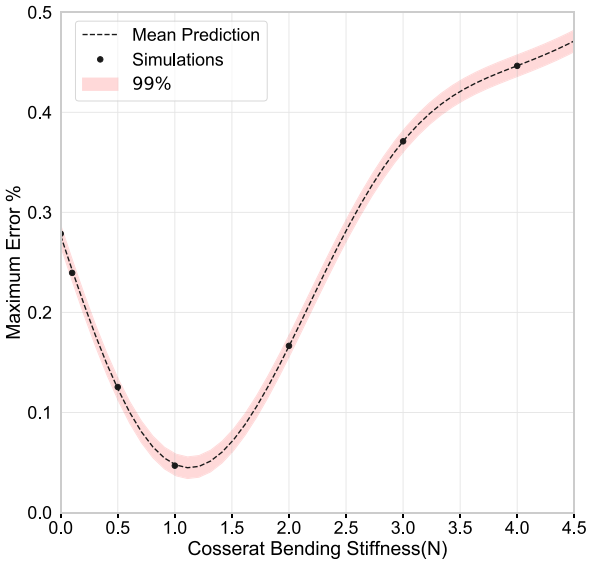

Fig. 3. Plot Cosserat bending stiffness β against maximum absolute error (%) $e(\beta)$.

To make this comparison the storage modulus from the simulations $\hat{E}(\ell_i, \beta)$ are calculated for a range of values of $\beta \in [0, 10]$ and each sample length ℓ_i. For each β the maximum absolute error $e(\beta)$ over all samples is calculated, given by

$$e(\beta) = \max_i \left| E(\ell_i) - \hat{E}(\ell_i, \beta) \right|. \tag{26}$$

To account for experimental measurement uncertainty, a 1D Gaussian process with a squared exponential kernel and free length scale parameter is fitted to the simulation/experiment comparison data. Fig. 3 shows the predict trend, confidence bounds and simulation outputs of β against $e(\beta)$. The results show that for a value $\beta \approx 1.2$N minimises the maximum absolute error between simulations and the experimental data set. This result highlights the new Cosserat formulation accurately captures the length dependency demonstrated by the experiments, achieving a small error percentage of $< 5\%$. This error is within the expected tolerance/variability of experimental measurements and could be refined further optimising other parameters in the model. For a non-Cosserat formulation, the error is significant ($> 30\%$), yet naturally this measure would increase further with more experiments of different length scales since the model's inability of capture the length dependency.

This numerical test also highlights another important aspect of the new Cosserat formulation. With the same setup a mesh convergence study for a single DMA sample of length $\ell = 5.32$ mm is performed for a Cosserat simulation with $\beta = 1$N and the non-Cosserat formulation. Fig. 4 demonstrates the superior converge rate of the Cosserat finite element solutions. This is expected, and represents the difference between quadratic (non-Cosserat) and cubic (Cosserat) converge. Importantly in larger scale manufacturing simulation, a single Cosserat element can be effectively used per ply/layer, because of the ability to accurately account for the bending response of the material. Therefore a given error, the superior converge properties of the element, mean that the additional Cosserat freedom (24 per element) are worth the computational investment.

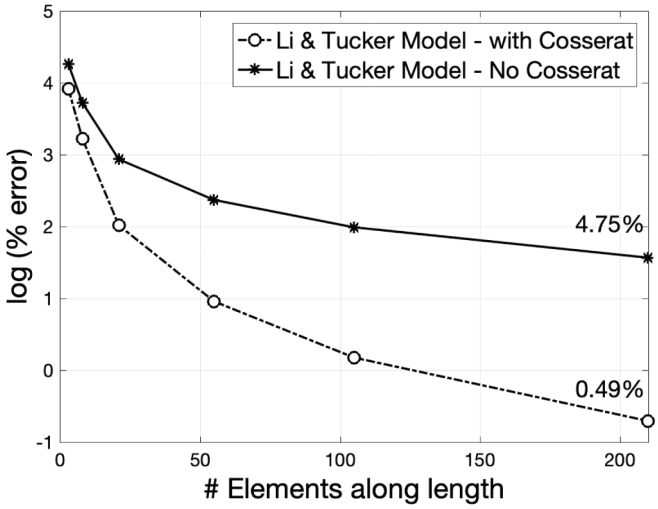

Fig. 4. A comparison showing the rate of superior rate of convergence of the Cosserat formula for DMA bending scenario over refinement of a standard quadratic element.

4.2. Internal fibre waviness/buckling

In the original composite process models, for example Li and Tucker III (2002), the mechanical response to compression and tension of a ply in the fibre direction was consider to be very stiff (proportional to the fibre stiffness) and symmetric (same in compression and tension). In practice whilst the tensile stiffness of ply in very high, if loaded in compression the fibres would become quickly buckle and causing the fibre waviness. Hence the response in compression and tension in practise is not symmetric. In this section, it is demonstrated how the Cosserat formulation accounts for this mechanics, where the original formulations fails, leading to pathological mesh dependent of the resulting waviness profiles.

In this numerical example, a single ply of composite is model which occupies the undeformed domain $\Omega_0 = 40 \times 8 \times 20$ mm, the domain is discretised into $10 \times 5 \times 4$ Cosserat elements. The same material parameters are used as the previous section with $\beta = 1$. The single ply, as shown in Fig. 5 is constrained with the following boundary conditions

$$\begin{cases} u_x = 0, & \theta_x = 0 \\ u_y = 0, & \theta_y = 0 \quad \text{at} \quad x = 0 \quad \text{and} \\ u_z = 0, & \theta_z = 0 \end{cases}$$
$$\begin{cases} u_x = -\Delta(t), & \theta_x = 0 \\ u_y = 0, & \theta_y = 0 \quad \text{at} \quad x = L \\ u_z = 0, & \theta_z = 0 \end{cases} \tag{27}$$
$$u_y = 0, \quad \theta_x = 0 \quad \theta_z = 0 \quad \text{at} \quad y = 0 \quad \text{and} \quad y = h$$
$$u_z = 0, \quad \theta_x = 0 \quad \theta_y = 0 \quad \text{at} \quad z = 0 \quad \text{and} \quad z = b.$$

These boundary conditions incrementally loads the ply in the fibre direction through a controlled displacement boundary condition.

Fig. 5 shows the load against strain response, as an internal wrinkling or buckling develops within constrained composite material when subjected to a compressive strain. The results show the response for $\beta = 0$ (Non-Cosserat) and $\beta = 1$. Both responses show a clear bifurcation/instability from a common fundamental compressive path (as highlighted by a dash response line). The clear difference between the two cases is the wavelength of the developed wrinkle. For the non-Cosserat formulation the wavelength complete coupled the mesh size, yet for $\beta = 1$ the introduction of a bending energy into the strain energy functional, means the profile develops are wavelength. This wavelength is independent of the mesh size.

The simulations are solutions of a complex nonlinear finite element scheme. To understand the mechanics behind the internal wrinkling, and the reasons for the mesh dependent wrinkle profiles observed in the non-Cosserat formulation, a simpler continuum model can be analysed. In this vein, a plane strain (x, z) section of a fibrous layer is considered of length L and height H. For simplicity of analysis, it is assumed all fibres align in the x direction, and the medium is in effect inextensible in x. The laminate is subject to a state of initial stress $\sigma_{11} = -\lambda$. Incremental displacements $w(x, z)$ in the z-direction away from the pre-stress state, give increments in stresses $s_{ij} = \Delta\sigma_{ij}$ and stress-couples $\mu = \Delta m_{12}$.

For a block of material of length L and height H is considered. Both vertical force and moment equilibrium can be written down, so that

$$\frac{ds_{21}}{dx} + \frac{ds_{22}}{dz} = \lambda \frac{dw}{dx} \quad \text{and} \quad s_{12} - s_{21} = \frac{d\mu}{dx}. \tag{28}$$

By rearranging and substituting one into the other we obtain the following differential equation

$$\frac{ds_{12}}{dx} - \frac{d^2\mu}{dx^2} + \frac{ds_{22}}{dz} = \lambda \frac{dw}{dx}. \tag{29}$$

For demonstration purposes it is possible to consider a much simpler, heuristic linear constitutive law which ignores Poisson effects. It therefore follows that

$$\mu = b\frac{d^2w}{dx^2}, \quad s_{12} = \hat{G}\frac{dw}{dx} \quad \text{and} \quad s_{22} = \hat{K}\frac{dw}{dz}, \tag{30}$$

where b is a Cosserat like bending stiffness, equivalent to β in the full nonlinear model. The parameters $\hat{G}$ and $\hat{K}$, are linear approximations of the shear stiffness and through-thickness compression. The equilibrium equations can be rewritten as

$$b\frac{d^4w}{dx^4} + (\lambda - \hat{G})\frac{d^2w}{dx^2} - \hat{K}\frac{d^2w}{dz^2} = 0. \tag{31}$$

To simplify the calculations we assume the incremental vertical displacement has the separable form

$$w(x, z) = W(x)\sin\left(\frac{\pi z}{H}\right).$$

Substituting this approximation into (31) and integrated z from 0 to H, we obtain the linear fourth-order ordinary differential equation

$$b\frac{d^4W}{dx^4} + (\lambda - \hat{G})\frac{d^2W}{dx^2} + kW = 0 \tag{32}$$

where $k = \hat{K}\pi^2/H^2$. Inserting the general solution $W(x) = Q\cos\omega x$, a characteristic equation is derived

$$2b\omega^2 = (\lambda - \hat{G}) \pm \sqrt{(\lambda - \hat{G})^2 - 4kb} \tag{33}$$

The Eq. (33) represent a curve in the (ω, λ) plane, which obtains a minimum at the critical load value

$$\lambda_c = 2\sqrt{kb} + \hat{G}. \tag{34}$$

This is the compressive stress $\lambda = \lambda_c$ at which a wrinkle defect will first initiate (a bifurcation), and has a corresponding half-wavelength of

$$\xi_c = \frac{\pi}{\omega_c} = \sqrt{\frac{2\pi^2 b}{\lambda_c - \hat{G}}} = \pi\left(\frac{b}{k}\right)^{1/4}. \tag{35}$$

Therefore the general form of the wrinkle at initiation is

$$w(x, z) = Q\cos\left(\frac{\pi x}{\xi}\right)\sin\left(\frac{\pi z}{H}\right), \quad \text{for} \quad x \in [0, L] \quad \text{and} \quad z \in [0, H].$$

The important observation in this paper is the relationship between b and ξ_c. As $b \to 0$, equivalent to $\beta \to 0$ in the fully-nonlinear Cosserat formulation, then the half-wavelength of the wrinkle $\xi_c \to 0$ as well. This is why, in the non-Cosserat formulation, the finite element solution attempts to replicate a wrinkle with infinitely small wavelength. With this, as the mesh is refined, the approximation on the finite element grid reduces accordingly, demonstrating a solution

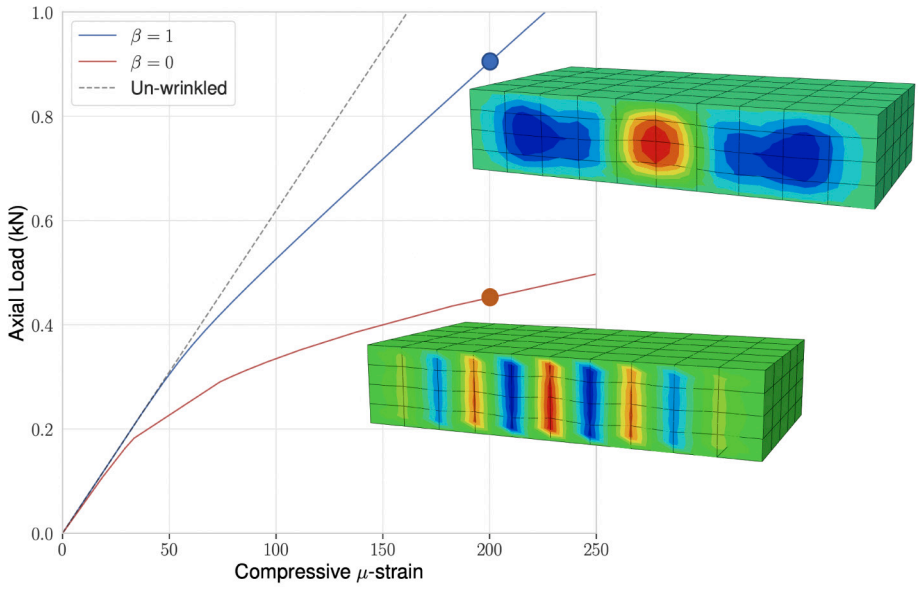

Fig. 5. Axial load against μ-strain curves for internal wrinkle for $\beta = 0$ (non-Cosserat) and $\beta = 1$. Inset plots shows, wrinkle profiles (scaled up) at 200 μ-strain. Importantly non-Cosserat solution, shows wavelength equal to mesh size, demonstrating clear mesh dependence.

with a wrinkle wavelength exactly matching the mesh . This is precisely what is observed in the solutions demonstrated by Li and Tucker III (2002, Fig. 10). With finite $b > 0$, a well-defined wrinkle wavelength is observed independent of the mesh size.

5. Composite manufacturing processes : Forming and consolidation

In this section, we present the application of the Cosserat model for two, small-scale manufacturing based scenarios of forming and consolidation examples. The results aim to demonstrate the capability of the new approach to model industry relevant cases. The scaling up of simulations to full scale components and manufacturing processes is discussed in Section 6.

5.1. Forming of L-shaped coupon

This example demonstrates the capability the new Cosserat element in Abaqus has to model a typical forming process. In doing so, various complex modelling challenges are introduced, including finite rotations and contact conditions between adjacent plies and with a tool surface. The simulation considers the forming of a L-shaped coupon over a rigid tool, for which the general setup and results are shown in Fig. 6. The rigid tool has a corner radius of 2.5 mm and is modelled by 200 linear, rigid, quadrilateral elements of type R3D4 in Abaqus. The three-dimensional deformable part is a block of $8 \times 2 \times 0.625$ mm dimension, and consists of three composite plies which are connected together with cohesive elements. Each ply is 0.2 mm thickness, and modelled by 56 user-defined Cosserat elements and accompanied by 56 quadratic hexahedral ghost elements of type C3D20. As highlighted above these are included for visualisation and implementation of contact algorithms. The material behaviour of the composite plies is the same as the problems in Section 4, and the initial fibre direction is along the length of the composite (forming around the corner). Each cohesive layer connecting the adjacent plies together has thickness of 0.0125 mm and is modelled using 224 linear 8-nodes hexahedral elements of type COH3D8 in Abaqus. The stiffness of cohesive material is 1 GPa in the normal direction to ply surface, while it is very compliant in shear with stiffness 0.1 MPa. The suggested value is inline with inter-ply shear experiments carried out by the authors (Erland et al., 2015). One end of the composite part is then fixed in all the directions, 1 atmos is applied to the top surface and the surface-to-surface frictionless contact was assumed at the interface between the bottom surface of composite and rigid tool surface.

Fig. 6 shows the forming solution in undeformed and deformed coordinates. The new higher-order Cosserat finite element has the ability to simulate the large deformation and rotation of the composite forming process. Qualitatively, the solutions clearly demonstrating the book-ending effect as expected (Dodwell, 2015). Future work will consider the upscaling of these simulations to large scale manufacturing processes, and with that validation against experimental forming demonstrators, each of which would be publications in their own right.

5.2. Large deformation consolidation of a corner radius

In this section, the three-dimensional Cosserat model is used to simulate the consolidation behaviour of composite laminates under the pressure from the autoclave process. The simulations use the same geometry that Li and Tucker used in their study (Li and Tucker III, 2002). The geometry of the consolidation case includes a 90° corner, as demonstrated in the results, Fig. 7. The initial configuration of the laminates is made form 24 plies with total thickness of 5.076 mm, each ply 0.2 mm thick and each cohesive layer 0.012 mm thick. The radius of the tool corner is 5 mm, and the length of the limb region is 50 mm. Material properties are taken to be the same as the previous sections (Table 1). In this study we demonstrate the flexibility of the ABAQUS model to investigate different stacking sequences, and therefore the simulations consider three different stacking sequences which are summarised in Table 2. In this case 90° plies run around the corner, 0° into the page and the normal directions is in the laminate stacking direction outwards from the internal radius of the (male) tool.

To simplify the example half the consolidated corner is modelled by apply symmetric boundary conditions at the apex of the corner. At the interface between the laminate and the tool surface , sliding boundary conditions are implemented. An autoclave pressure is applied on the outer side of the laminates surface, which is linearly ramped from 0 to 0.5 MPa (5 bar). At the free end a no-pressure (homogeneous Neumann) boundary is applied on end of the laminate. The complete model consists of 2392 linear hexahedral elements of type COH3D8 for the cohesive layers, 624 user-defined Cosserat elements and a matching

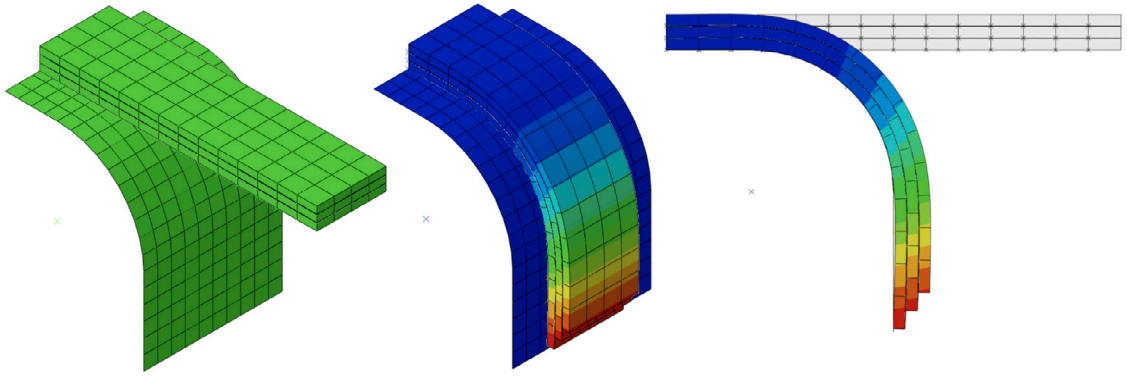

Fig. 6. Deformed configuration of bending the three-layer composite stack over 90 degree corner, (a) three dimensional view, and (b) side view.

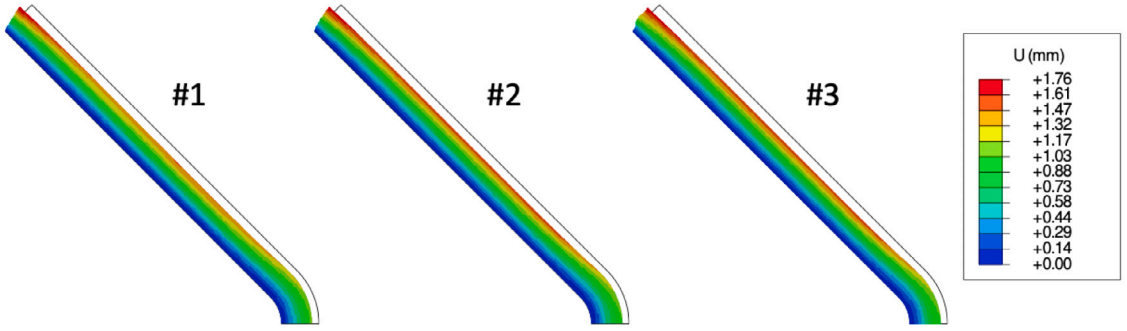

Fig. 7. Consolidation profiles for three different stacking sequences as presented in Table 2. Stacking sequence shows clear effect on the shear profile ('book-ending') for each case. Cosserat FEM formulation, displays no mesh dependent instabilities as presented in results for Li and Tucker III (2002).

Table 2
Three symmetric, 24 ply, quasi-isotropic stacking sequences consider in consolidation simulations (○ = 0°, • = 90°, + = 45° and − = −45°).

ID	Stacking sequence
1	+/−/+/−/+/−/○/•/○/•/○/•/•/○/•/○/•/○/−/+/−/+/−/+
2	+/○/−/•/+/○/−/•/+/○/−/•/•/−/○/+/•/−/○/+/•/−/○/+
3	+/○/+/○/+/○/−/•/−/•/−/•/•/−/•/−/•/−/○/+/○/+/○/+

624 quadratic hexahedral ghost elements of type C3D20. Each ply is modelled with a single 3D Cosserat element, as shown in Fig. 2, through thickness and approximately square in-plane. In total, a simulation has 3052 elements (with 54k degrees of freedom).

Fig. 7 shows the consolidation profiles of each of the three stacking sequences. In general the response is similar, we observe consolidation of approximately 18% around the corner radius, which increases to as much as 35% at the free edge. An interesting observation is that in the Li and Tucker III (2002) paper 'wiggles' are observed in the corner region under a similar consolidation process. They suggest that it is due to the generation of wrinkles in the fibrous laminates, similar to the internal wrinkling mechanics reported in Section 4.2. However, as they report, the wrinkles dependent (and exactly the size) of the mesh. Using the regularised Cosserat formulation introduced in this paper, no such mesh dependent wrinkles are observed, which is what one would expect physically in a relatively thin laminate consolidation setup.

6. Conclusions and further avenues for research

This paper presents a new three dimensional, finite deformation Cosserat continuum model for uncured carbon fibre composites. The resulting continuum model captures the bending contributions of stiff carbon fibres at the microscale within the continuum description of the problem. The paper demonstrates the inclusion of such mechanics is essential in order to accurately model various bending responses of the material during typical manufacturing processes. This includes large deformation forming, finite strain consolidation and wrinkling (the formation of an unwanted defect). If such mechanics are not included at the macroscale, the literature demonstrates the resulting finite element solutions have a pathological dependence on the mesh size, requiring researchers to fit mesh dependent material parameters, which limits confidence in their predictive capabilities.

To include the effect of fibre bending stiffness in the ply level material behaviour, a new anisotropic hyperelastic continuum model for the material which includes a higher-order term dependent on the curvature of the material in the fibre direction is developed. With this a higher-order, Taylor-Hood Cosserat finite element is introduced, and implemented within the commercial code Abaqus as a new User-Defined Element (UEL) (and material model embedded within it). This will be made available on request to the authors.

The paper then considers a series of simulations to demonstrate and validate the new mechanics of the Cosserat element. Firstly, simulations are compared with Dynamical Mechanical Analysis tests of the material to experimentally fit the new Cosserat bending stiffness β. The Cosserat model then demonstrates the ability to capture fibre wrinkling mechanics under axial compression of the fibrous material, without dependence on the finite element mesh. Finally, by implementing the model within Abaqus and few implementation tricks (described above) the new modelling framework can readily utilise more general modelling capabilities which include complex geometry, boundary conditions, cohesive ply-to-ply slip and non-local contact. This additional flexible enables the paper to demonstrates two small-scale manufacturing test cases (i) forming of an L-shape sample and (ii) consolidation of an external radius. It is worth mentioning that the users of this model should provide special attention to define the contact approach and defining the mesh size for the contact region as using quadratic element might cause special problems in Abaqus in some cases with the node-to-surface formulation. This problem is due to generation

of an ambiguous force on the corner nodes on the face of second-order element without midface node. This is sometimes automatically solved by Abaqus by converting the three-dimensional second-order elements into the elements with midface nodes. However, when this is not possible, the user should specify a penalty or augmented Lagrange constraint enforcement method to approximate this behaviour.

The final results, which demonstrate the potential to model real manufacturing processes, open new fruitful (both theoretical and applied) research to increase their applicability within the composite industry and in general other research fields (e.g. geoscience). The authors see three areas of mid-term development of the work presented in this paper:

- **Scaling up to large components.** The formulation presented still models an individual ply. As a results simulations quickly become computationally expensive, since the thickness of an individual layer ($\sim$ 0.2 mm) is so much smaller than even a moderate composite component. Therefore, a natural area to extend the work presented in this paper is to upscale the Cosserat element, to define a laminate scale (multiple plies) formulation. In a simplified small strain setting this has been demonstrated by one of the authors (Dodwell, 2015). Here, a simple approach worthy of investigation is to use a basic upscaling scheme, akin to that used in multiple composite elements for cured stress analysis. In simple terms, integration points are placed at locations of plies internal to that element, and the results macroscale element has the approximate average stiffness at the macroscale. This basic approach will come with approximation errors, and its validity as a method will depend on how well the modes of deformation of the stack are captured by a single higher-order element at the macroscale.
- **Flexibility to add additional physics from other models in the literature.** A key aspect of the modelling approach is the Cosserat component is a single additive term to the strain energy functional alongside a quadratic constraint term. Therefore it's formulation, whilst demonstrate with Li and Tucker III (2002) choice of anisotropic model could be adopted by other models. This includes adding the important effects of resin fusion, cure kinetics and temperature distribution.
- **Industry-focused toolbox in Abaqus — Cae.** Since the 1960s Cosserat models have periodically re-appeared in various academic fields, most notably in geomechanics Adhikary and Dyskin (1997) and Mühlhaus et al. (2002). However, often they have obtained little traction long term, except for in more academic modelling contributions. The authors believe the reason for this is the lack of availability of implementations within commercial finite element packages like Abaqus. Therefore large upfront investment is required by a research group to implement their own code. This paper overcomes many of these hurdles, by providing details (and code on request) of the required Abaqus user-defined element UEL. Ongoing work is further increasing the usability of the new model, by embedding the Cosserat element as a toolbox with Abaqus-CAE. This will remove the need of engineering users to detail with the Fortran code directly.

Declaration of competing interest

The authors declare that they have no known competing financial interests or personal relationships that could have appeared to influence the work reported in this paper.

Acknowledgements

This work was supported under the EPSRC, UK grant 'Analysis and Design for Accelerated Production and Tailoring of composites (ADAPT)' (EP/N024508/1). Professor Tim Dodwell is supported by a Turing AI Fellowship, UK (2TAFFP\100007).

Appendix. Detailed calculations for finite strains Cosserat material model for uncured composites

This section provides the derivation of the symmetric part of Cauchy stress, $\boldsymbol{\sigma}_{sym}$, the deviatoric part of couple stress, $\overline{\mathbf{m}}$ and the fourth-order Lagrangian elastic tensor $\mathbb{C}_{\sigma}$ and $\mathbb{C}_{\mathbf{m}}$. Starting from the strain energy functional (Eq. (6)) in Section 2:

$$W = W_0(\mathcal{L}) + \frac{E_s\phi_0}{4}(L - \ln L) + \frac{G}{2}(I_1 - 3) - G(\ln J) + \frac{K}{2}(\ln J)^2 + \beta\left(\underbrace{\mathbf{e}^0\cdot\boldsymbol{\Lambda}^{\mathrm{T}}\boldsymbol{\Lambda}\cdot\mathbf{e}^0}_{:=I_6}\right)$$

which is a function of deformation invariants, $I_1 = \mathrm{tr}(\mathbf{C})$, $J = \det(\mathbf{F})$, $L = (\mathbf{e}^0\otimes\mathbf{e}^0)\cdot\mathbf{C}$, $\mathcal{L} = (\mathbf{n}^0\otimes\mathbf{n}^0)\cdot\mathbf{C}^{-1}$, and $I_6 = \mathbf{e}^0\cdot\boldsymbol{\Lambda}^{\mathrm{T}}\boldsymbol{\Lambda}\cdot\mathbf{e}^0$. In Section 2, the Cauchy stress, $\boldsymbol{\sigma}_{sym}$, and the deviatoric part of couple stress, $\overline{\mathbf{m}}$ are related to strain energy functional through the following relationships

$$\boldsymbol{\sigma}_{sym} = \frac{2}{J}\mathbf{F}\frac{\partial W}{\partial \mathbf{C}}\mathbf{F}^{\mathrm{T}} \quad \text{and} \quad \overline{\mathbf{m}} = \frac{1}{J}\mathbf{F}\frac{\partial W}{\partial \boldsymbol{\Lambda}}\mathbf{F}^{\mathrm{T}}. \tag{36}$$

and the fourth-order Lagrangian elastic tensor $\mathbb{C}_{\sigma}$ and $\mathbb{C}_{\mathbf{m}}$, which connects coupled stress $\mathbf{m}$ to the curvatures measure $\boldsymbol{\Lambda}$, are derived from

$$\mathbb{C}_{\sigma} = 4\frac{\partial^2 W}{\partial\mathbf{C}\partial\mathbf{C}} \quad \text{and} \quad \mathbb{C}_{\mathbf{m}} = \frac{\partial^2 W}{\partial\boldsymbol{\Lambda}\partial\boldsymbol{\Lambda}}. \tag{37}$$

The first derivative of strain energy function with respect to $\mathbf{C}$ and $\boldsymbol{\Lambda}$ are as follow s

$$\frac{\partial W}{\partial \mathbf{C}} = \frac{\partial W_0(\mathcal{L})}{\partial\mathcal{L}}\frac{\partial\mathcal{L}}{\partial\mathbf{C}} + \frac{E_s\phi_0}{4}\left(1-\frac{1}{L}\right)\frac{\partial L}{\partial\mathbf{C}} + \frac{G}{2}\frac{\partial I_1}{\partial\mathbf{C}} - \frac{G}{J}\frac{\partial J}{\partial\mathbf{C}} + \frac{K}{J}\ln J\frac{\partial J}{\partial\mathbf{C}} + \beta\frac{\partial I_6}{\partial\mathbf{C}}, \tag{38}$$

and

$$\frac{\partial W}{\partial \boldsymbol{\Lambda}} = \frac{\partial W_0(\mathcal{L})}{\partial\mathcal{L}}\frac{\partial\mathcal{L}}{\partial\boldsymbol{\Lambda}} + \frac{E_s\phi_0}{4}\left(1-\frac{1}{L}\right)\frac{\partial L}{\partial\boldsymbol{\Lambda}} + \frac{G}{2}\frac{\partial I_1}{\partial\boldsymbol{\Lambda}} - \frac{G}{J}\frac{\partial J}{\partial\boldsymbol{\Lambda}} + \frac{K}{J}\ln J\frac{\partial J}{\partial\boldsymbol{\Lambda}} + \beta\frac{\partial I_6}{\partial\boldsymbol{\Lambda}}, \tag{39}$$

for which

$$\frac{\partial W_0}{\partial\mathcal{L}} = \frac{A_s}{2}\frac{\mathcal{L}-\sqrt{\mathcal{L}}}{(\frac{1}{\phi_0}-\frac{\sqrt{\mathcal{L}}}{\phi_a})^4} + \frac{G-G_0}{2}(\frac{1}{\mathcal{L}^2}-\frac{1}{\mathcal{L}}).$$

Therefore, by replacing the derivatives of invariants from Table 3 it follows that

$$\frac{\partial W}{\partial \mathrm{C}_{ij}} = -\left[\frac{A_s}{2}\frac{\mathcal{L}-\sqrt{\mathcal{L}}}{(\frac{1}{\phi_0}-\frac{\sqrt{\mathcal{L}}}{\phi_a})^4} + \frac{G-G_0}{2}(\frac{1}{\mathcal{L}^2}-\frac{1}{\mathcal{L}})\right]\mathbf{n}^0_p\mathbf{n}^0_q\mathrm{C}^{-1}_{pi}\mathrm{C}^{-1}_{jq} + \frac{E_s\phi_0}{4}(1-\frac{1}{L})\mathbf{e}^0_i\mathbf{e}^0_j + \frac{1}{2}G\left(\delta_{ij}-\mathrm{C}^{-1}_{ij}\right) + \frac{K}{2}\ln J\mathrm{C}^{-1}_{ij}, \tag{40}$$

and

$$\frac{\partial W}{\partial \Lambda_{ij}} = 2\beta\Lambda_{ik}\mathrm{e}^0_k\mathrm{e}^0_j. \tag{41}$$

Furthermore by replacing the Eqs. (40) and (41) in (36), the $\boldsymbol{\sigma}_{sym}$, and $\overline{\mathbf{m}}$ are given by

$$\boldsymbol{\sigma}_{(ij)} = \frac{2}{J}\mathrm{F}_{im}\left\{-\left[\frac{A_s}{2}\frac{\mathcal{L}-\sqrt{\mathcal{L}}}{(\frac{1}{\phi_0}-\frac{\sqrt{\mathcal{L}}}{\phi_a})^4} + \frac{G-G_0}{2}\left(\frac{1}{\mathcal{L}^2}-\frac{1}{\mathcal{L}}\right)\right]\mathbf{n}^0_p\mathbf{n}^0_q\mathrm{C}^{-1}_{pm}\mathrm{C}^{-1}_{nq} + \frac{E_s\phi_0}{4}\left(1-\frac{1}{L}\right)\mathbf{e}^0_m\mathbf{e}^0_n + \frac{1}{2}G\left(\delta_{mn}-\mathrm{C}^{-1}_{mn}\right) + \frac{K}{2}\ln J\mathrm{C}^{-1}_{mn}\right\}\mathrm{F}_{jn}, \tag{42}$$

and

$$\overline{\mathrm{m}}_{ij} = \frac{2\beta}{J}\mathrm{F}_{im}(\Lambda_{mk}\mathrm{e}^0_k\mathrm{e}^0_n)\mathrm{F}_{jn}. \tag{43}$$

Table 3
First and second derivatives of invariants with respect to $\mathbf{C}$ and $\mathbf{\Lambda}$.

$\frac{\partial I_1}{\partial \mathbf{C}} = \mathbf{I}$	$\frac{\partial I_1}{\partial \mathbf{\Lambda}} = \mathbf{0}$	$\frac{\partial^2 I_1}{\partial C_{ij}\partial C_{kl}} = 0_{ijkl}$	$\frac{\partial^2 I_1}{\partial \Lambda_{ij}\partial \Lambda_{kl}} = 0_{ijkl}$
$\frac{\partial J}{\partial \mathbf{C}} = \frac{1}{2} J\mathbf{C}^{-1}$	$\frac{\partial J}{\partial \mathbf{\Lambda}} = \mathbf{0}$	$\frac{\partial^2 J}{\partial C_{ij}\partial C_{kl}} = \frac{1}{2}\left[\frac{1}{2} J C^{-1}_{ij} C^{-1}_{kl} - J C^{-1}_{ik} C^{-1}_{lj}\right]$	$\frac{\partial^2 J}{\partial \Lambda_{ij}\partial \Lambda_{kl}} = 0_{ijkl}$
$\frac{\partial L}{\partial C_{ij}} = \mathbf{e}^0 \otimes \mathbf{e}^0$	$\frac{\partial L}{\partial \mathbf{\Lambda}} = \mathbf{0}$	$\frac{\partial^2 L}{\partial C_{ij}\partial C_{kl}} = 0_{ijkl}$	$\frac{\partial^2 L}{\partial \Lambda_{ij}\partial \Lambda_{kl}} = 0_{ijkl}$
$\frac{\partial \mathcal{L}}{\partial C_{ij}} = -\left(\mathbf{C}^{-T}\mathbf{n}\right) \otimes \left(\mathbf{C}^{-1}\mathbf{n}\right)$	$\frac{\partial \mathcal{L}}{\partial \mathbf{\Lambda}} = \mathbf{0}$	$\frac{\partial^2 \mathcal{L}}{\partial C_{ij}\partial C_{kl}} = \mathbf{n}^0_p \mathbf{n}^0_q \left(C^{-1}_{pi} C^{-1}_{jk} C^{-1}_{lq} + C^{-1}_{pk} C^{-1}_{li} C^{-1}_{jq}\right)$	$\frac{\partial^2 \mathcal{L}}{\partial \Lambda_{ij}\partial \Lambda_{kl}} = 0_{ijkl}$
$\frac{\partial I_6}{\partial \mathbf{C}} = \mathbf{0}$	$\frac{\partial I_6}{\partial \mathbf{\Lambda}} = 2\mathbf{\Lambda}\left(\mathbf{e}^0 \otimes \mathbf{e}^0\right)$	$\frac{\partial^2 I_6}{\partial C_{ij}\partial C_{kl}} = 0_{ijkl}$	$\frac{\partial^2 I_6}{\partial \Lambda_{ij}\partial \Lambda_{kl}} = 2\left(\mathbf{e}^0_i \mathbf{e}^0_j\right)\delta_{kl}$

Similarly, to compute the fourth-order elastic tensors $\mathbb{C}_\sigma$ and $\mathbb{C}_\mathbf{m}$, the second derivatives of the strain energy functional are calculated so that

$$\begin{aligned}\frac{\partial^2 W}{\partial \mathbf{C}\partial \mathbf{C}} = {} & \frac{\partial^2 W_0}{\partial \mathcal{L}^2}\left(\frac{\partial \mathcal{L}}{\partial \mathbf{C}} \otimes \frac{\partial \mathcal{L}}{\partial \mathbf{C}}\right) + \frac{\partial W_0}{\partial \mathcal{L}}\frac{\partial}{\partial \mathbf{C}}\left(\frac{\partial \mathcal{L}}{\partial \mathbf{C}}\right) \\ & + \frac{E_s \phi_0}{4}\left(\frac{\partial^2 L}{\partial \mathbf{C}^2} - \frac{1}{L}\frac{\partial^2 L}{\partial \mathbf{C}^2} + \frac{1}{L^2}\left(\frac{\partial L}{\partial \mathbf{C}} \otimes \frac{\partial L}{\partial \mathbf{C}}\right)\right) \\ & + \frac{G}{2}\frac{\partial^2 I_1}{\partial \mathbf{C}^2} - G\left(\frac{1}{J}\frac{\partial^2 J}{\partial \mathbf{C}^2} - \frac{1}{J^2}\left(\frac{\partial J}{\partial \mathbf{C}} \otimes \frac{\partial J}{\partial \mathbf{C}}\right)\right) \\ & + K\left(\frac{1 - \ln J}{J^2}\left(\frac{\partial J}{\partial \mathbf{C}} \otimes \frac{\partial J}{\partial \mathbf{C}}\right) + \frac{1}{J}\frac{\partial^2 J}{\partial \mathbf{C}^2}\right),\end{aligned} \tag{44}$$

and

$$\frac{\partial^2 W}{\partial \mathbf{\Lambda}\partial \mathbf{\Lambda}} = \frac{\partial^2 W}{\partial \mathbf{\Lambda}^2} = 2\beta\left(\mathbf{e}^0 \otimes \mathbf{e}^0\right) \otimes \mathbf{I}. \tag{45}$$

Finally, by replacing the first and second derivation of invariants from Table 3 into Eqs. (44) and (45), following the form for $\mathbb{C}_\sigma$ and $\mathbb{C}_\mathbf{m}$ that is implemented in the user-defined element in Abaqus, it follows that

$$\begin{aligned}\mathbb{C}_{\sigma_{ijkl}} = {} & \left\{ \frac{A_s}{2}\left[\frac{(1 - \frac{1}{2\sqrt{\mathcal{L}}})(\frac{1}{\phi_0} - \frac{\sqrt{\mathcal{L}}}{\phi_a}) - \frac{2\left(\mathcal{L} - \sqrt{\mathcal{L}}\right)}{\phi_a \sqrt{\mathcal{L}}}}{(\frac{1}{\phi_0} - \frac{\sqrt{\mathcal{L}}}{\phi_a})^5}\right] \right. \\ & \left. + \frac{G - G_0}{2}\left(\frac{1}{\mathcal{L}^2} - \frac{2}{\mathcal{L}^3}\right)\right\}\left(\mathbf{n}^0_p \mathbf{n}^0_q C^{-1}_{pi} C^{-1}_{jq}\right)\left(\mathbf{n}^0_m \mathbf{n}^0_n C^{-1}_{mk} C^{-1}_{ln}\right) + \\ & \left[\frac{A_s}{2}\frac{\mathcal{L} - \sqrt{\mathcal{L}}}{(\frac{1}{\phi_0} - \frac{\sqrt{\mathcal{L}}}{\phi_a})^4} + \frac{G - G_0}{2}\left(\frac{1}{\mathcal{L}^2} - \frac{1}{\mathcal{L}}\right)\right] \\ & \times\left(\mathbf{n}^0_p \mathbf{n}^0_q C^{-1}_{pi} C^{-1}_{jk} C^{-1}_{lq} + \mathbf{n}^0_m \mathbf{n}^0_n C^{-1}_{mk} C^{-1}_{li} C^{-1}_{jn}\right) + \frac{E_s \phi_0}{4L^2}\left(\mathbf{e}^0_i \mathbf{e}^0_j \mathbf{e}^0_k \mathbf{e}^0_l\right) + \\ & \frac{G}{2} C^{-1}_{ik} C^{-1}_{lj} + \frac{K}{4} C^{-1}_{ij} C^{-1}_{kl} - \frac{K}{2} \ln J C^{-1}_{ik} C^{-1}_{lj}\end{aligned} \tag{46}$$

and

$$\mathbb{C}_{\mathbf{m}_{ijkl}} = 2\beta\left(\mathbf{e}^0_i \mathbf{e}^0_j\right)\delta_{kl}. \tag{47}$$

References

Abaqus, 2014. 6.14 documentation. Dassault Systemes Simulia Corporation 651.

Adhikary, D., Dyskin, A., 1997. A cosserat continuum model for layered materials. Comput. Geotech. 20 (1), 15–45.

Askes, H., Aifantis, E.C., 2011. Gradient elasticity in statics and dynamics: an overview of formulations, length scale identification procedures, finite element implementations and new results. Int. J. Solids Struct. 48 (13), 1962–1990.

Belnoue, J.P.-H., Hallett, S.R., 2020. A rapid multi-scale design tool for the prediction of wrinkle defect formation in composite components. Mater. Des. 187, 108388.

Belnoue, J.P.-H., Mesogitis, T., Nixon-Pearson, O.J., Kratz, J., Ivanov, D.S., Partridge, I.K., Potter, K.D., Hallett, S.R., 2017. Understanding and predicting defect formation in automated fibre placement pre-preg laminates. Composites A 102, 196–206.

Belnoue, J.-H., Nixon-Pearson, O., Ivanov, D., Hallett, S., 2016. A novel hyper-viscoelastic model for consolidation of toughened prepregs under processing conditions. Mech. Mater. 97, 118–134.

Belnoue, J.-H., Nixon-Pearson, O., Thompson, A., Ivanov, D., Potter, K., Hallett, S., 2018. Consolidation-driven defect generation in thick composite parts. J. Manuf. Sci. Eng. 140 (7), 071006.

Bigoni, D., Gourgiotis, P.A., 2016. Folding and faulting of an elastic continuum. Proc. R. Soc. A 472 (2187), 20160018.

Boisse, P., Colmars, J., Hamila, N., Naouar, N., Steer, Q., 2018a. Bending and wrinkling of composite fiber preforms and prepregs, a review and new developments in the draping simulations. Composites B 141, 234–249.

Boisse, P., Hamila, N., Madeo, A., 2018b. The difficulties in modeling the mechanical behavior of textile composite reinforcements with standard continuum mechanics of cauchy, some possible remedies. Int. J. Solids Struct. 154, 55–65.

Bonet, J., Wood, R.D., 1997. Nonlinear Continuum Mechanics for Finite Element Analysis. Cambridge university press.

Composites Leadership Forum, 2016. The 2016 UK Composites Strategy: Delivering UK growth through the multi-sector application of composites. https://compositesuk.co.uk/system/files/documents/Strategy final version_1.pdf.

Cosserat, E, Cosserat, F, 1909. Theory of deformable bodies, scientific library, a. Hermann and Sons, Paris.

Dodwell, T., 2015. Internal wrinkling instabilities in layered media. Phil. Mag. 95 (28–30), 3225–3243.

Dodwell, Tim J, Kinston, S, Butler, Richard, Haftka, Raphael T, Kim, Nam H, Scheichl, Robert, 2019. Multilevel monte carlo simulations of composite structures with uncertain manufacturing defects. arXiv preprint arXiv:1907.10271.

Erland, S., 2017. Characterisation of Uncured Carbon Fibre Prepreg (Ph.D. thesis). University of Bath.

Erland, S., Dodwell, T., Butler, R., 2015. Characterisation of inter-ply shear in uncured carbon fibre prepreg. Composites A 77, 210–218.

Fedorova, S., Lasota, T., Burša, J., 2016. Computational modeling of fiber composites with thick fibers as homogeneous structures with use of couple stress theory. In: Design and Analysis of Reinforced Fiber Composites. Springer, pp. 25–47.

Fernlund, G., Griffith, J., Courdji, R., Poursartip, A., 2002. Experimental and numerical study of the effect of caul-sheets on corner thinning of composite laminates. Composites A 33 (3), 411–426.

Forest, S., 1998. Modeling slip, kink and shear banding in classical and generalized single crystal plasticity. Acta Mater. 46 (9), 3265–3281.

Forest, S., Barbe, F., Cailletaud, G., 2000. Cosserat modelling of size effects in the mechanical behaviour of polycrystals and multi-phase materials. Int. J. Solids Struct. 37 (46–47), 7105–7126.

Froiio, F., Tomassetti, G., Vardoulakis, I., 2006. Mechanics of granular materials: the discrete and the continuum descriptions juxtaposed. Int. J. Solids Struct. 43 (25–26), 7684–7720.

Gutowski, T.G., Cai, Z., Bauer, S., Boucher, D., Kingery, J., Wineman, S., 1987. Consolidation experiments for laminate composites. J. Compos. Mater. 21 (7), 650–669.

Hallander, P., Sjölander, J., Petersson, M., Åkermo, M., 2016. Interface manipulation towards wrinkle-free forming of stacked ud prepreg layers. Composites A 90, 340–348.

Hubert, P., Vaziri, R., Poursartip, A., 1999. A two-dimensional flow model for the process simulation of complex shape composite laminates. Internat. J. Numer. Methods Engrg. 44 (1), 1–26.

Hunt, G., Dodwell, T., Hammond, J., 2013. On the nucleation and growth of kink and shear bands. Phil. Trans. R. Soc. A 371 (1993), 20120431.

Lakes, R., 1995. Experimental methods for study of cosserat elastic solids and other generalized elastic continua. Contin. Models Mater. Microstruct. 1–25.

Li, Y., Li, M., Gu, Y., Zhang, Z., 2009. Numerical and experimental study on the effect of lay-up type and structural elements on thickness uniformity of l-shaped laminates. Appl. Compos. Mater. 16 (2), 101–115.

Li, M., Tucker III, C.L., 2002. Modeling and simulation of two-dimensional consolidation for thermoset matrix composites. Composites A 33 (6), 877–892.

Lightfoot, J.S., Wisnom, M.R., Potter, K., 2013. A new mechanism for the formation of ply wrinkles due to shear between plies. Composites A 49, 139–147.

Limbert, G., Middleton, J., 2004. A transversely isotropic viscohyperelastic material: Application to the modeling of biological soft connective tissues. Int. J. Solids Struct. 41 (15), 4237–4260.

Madeo, A., Ferretti, M., Dell'Isola, F., Boisse, P., 2015. Thick fibrous composite reinforcements behave as special second-gradient materials: three-point bending of 3d interlocks. Z. Angew. Math. Phys. 66 (4), 2041–2060.

Maugin, G.A., 2017. Non-Classical Continuum Mechanics. Springer.

Mühlhaus, H.-B., Dufour, F., Moresi, L., Hobbs, B., 2002. A director theory for visco-elastic folding instabilities in multilayered rock. Int. J. Solids Struct. 39 (13–14), 3675–3691.

Pavliotis, G., Stuart, A., 2008. Multiscale Methods: Averaging and Homogenization. Springer Science & Business Media.
Ropers, S., Kardos, M., Osswald, T.A., 2016. A thermo-viscoelastic approach for the characterization and modeling of the bending behavior of thermoplastic composites. Composites A 90, 22–32.
Sachs, U., Akkerman, R., 2017. Viscoelastic bending model for continuous fiber-reinforced thermoplastic composites in melt. Composites A 100, 333–341.
Sandhu, A., Reinarz, A., Dodwell, T., 2018. A bayesian framework for assessing the strength distribution of composite structures with random defects. Compos. Struct. 205, 58–68.
Spencer, A., Soldatos, K., 2007. Finite deformations of fibre-reinforced elastic solids with fibre bending stiffness. Int. J. Non-Linear Mech. 42 (2), 355–368.
Sutcliffe, M., 2013. Modelling the effect of size on compressive strength of fibre composites with random waviness. Compos. Sci. Technol. 88, 142–150.
Tejchman, J., Wu, W., 1993. Numerical study on patterning of shear bands in a cosserat continuum. Acta Mech. 99 (1–4), 61–74.
Varkonyi, B., Belnoue, J.P.-H., Kratz, J., Hallett, S.R., 2019. Predicting consolidation-induced wrinkles and their effects on composites structural performance. Int. J. Mater. Form. 1–15.
Wang, X., Zhang, Z., Xie, F., Li, M., Dai, D., Wang, F., 2009. Correlated rules between complex structure of composite components and manufacturing defects in autoclave molding technology. J. Reinforced Plast. Compos. 28 (22), 2791–2803.
Zienkiewicz, O.C., Taylor, R.L., 1994. The Finite Element Method: Basic Formulation and Linear Problems, Vol. 1. McGraw-Hill Berkshire, UK.